Chemical Engineering Journal 420 (2021) 127597

Contents lists available at ScienceDirect

Chemical Engineering Journal

journal homepage: www.elsevier.com/locate/cej

Ultra-strong capillarity of bioinspired micro/nanotunnels in organic cathodes enabled high-performance all-organic sodium-ion full batteries

Gangyong Zhou [a], Lulu Mo [a], Chunyang Zhou [a], Yue Wu [d], Feili Lai [c], Yan Lv [a], Jianmin Ma [b], Yue-E Miao [a,*], Tianxi Liu [a,*]

[a] State Key Laboratory for Modification of Chemical Fibers and Polymer Materials, College of Materials Science and Engineering, Innovation Center for Textile Science and Technology, Donghua University, Shanghai 201620, PR China
[b] School of Physics and Electronics, Hunan University, Changsha 410082, PR China
[c] Department of Chemistry, KU Leuven, Celestijnenlaan 200F, Leuven 3001, Belgium
[d] Research Center for Analysis and Measurement, Donghua University, Shanghai 201620, PR China

ARTICLE INFO

Keywords:
Organic cathode
Electrospinning
Bio-inspired
Hierarchical micro/nanotunnels
Sodium-ion full battery

ABSTRACT

As one of the typical organic cathode materials for sodium ion batteries (SIBs), 3,4,9,10-perylenetetracarboxylic dianhydride (PTCDA) is formidably challenged in practical applications because of its low electrical conductivity, sluggish reaction kinetics, inferior rate capability and cycle life. Inspired by the ultra-strong capillarity of wood's aligned hierarchical microchannels toward ions and water during metabolism, we have designed a novel composite nanofibrous organic cathode consisting of PTCDA/nitrogen-doped carbon/carbon nanotubes (PTCDA/NC/CNT) for SIBs. The PTCDA/NC/CNT cathode exhibits rapid ionic/electronic transport properties and ultrafast reaction kinetics owing to the synergistic effects of the interconnected conductive frameworks and ultrastrong capillarity deriving from the hierarchical micro/nanotunnels. As a result, a highly reversible capacity of 135.6 mA h g^{-1} at 50 mA g^{-1}, excellent rate performance and ultra-long cyclic stability with over 95% capacity retention after 500 cycles at 1000 mA g^{-1} are achieved for the PTCDA/NC/CNT cathode in SIBs. Remarkably, an all-organic battery using the PTCDA/NC/CNT cathode and conjugated sodium carboxylate/CNT anode also delivers a high energy density of 85 W h kg^{-1} at a power density of 665 W kg^{-1}. This bio-inspired design provides a promising strategy for the development of next-generation all-organic sodium-ion full batteries.

1. Introduction

Rechargeable sodium-ion batteries (SIBs) have been regarded as one kind of the most promising candidates instead of the conventional lithium-ion batteries (LIBs) due to the advantages of abundant sodium resources, low cost and environmental friendliness [1–8]. Unfortunately, most of the current SIBs assembled with inorganic electrode materials exhibit low specific capacity, poor cycle life and inferior rate performance because of the intrinsic large ionic radius of sodium, which will lead to multistep phase transitions, severe volume expansion and even electrode structure collapse during the discharge/charge processes [9–15]. In contrast, organic materials show great superiorities in good tolerance for cationic radius as well as structural designability, sustainable resources and environmental friendliness, which should be one kind of the most hopeful electrode materials for green and sustainable SIBs [16–19]. To date, several types of organic materials have been reported for constructing SIB electrodes, such as organosulphur compounds [20,21], conducting polymers [22,23], organic radical compounds [24,25] and carbonyl compounds [18,26–29]. Among them, conjugated carbonyl compounds are most widely used due to their plenty of electroactive functional groups (C═O), tunable redox potentials and good accessibility [26–30]. As a typical superconjugated carbonyl compound, 3,4,9,10-perylenetetracarboxylic dianhydride (PTCDA) can associate/disassociate with Na^+ reversibly and maintain the stable molecular structure during discharge/charge processes [26,31]. However, most of the current PTCDA-based cathodes are simply fabricated by mechanically blending with conductive additives and polymer binders, which generate poor mechanical properties, inferior rate performance and limited capacity due to the slow ionic/electronic transport and the sluggish reaction kinetics of Na^+ within the powdery

* Corresponding authors.
E-mail addresses: yuee_miao@dhu.edu.cn (Y.-E. Miao), txliu@dhu.edu.cn (T. Liu).

https://doi.org/10.1016/j.cej.2020.127597
Received 13 August 2020; Received in revised form 21 October 2020; Accepted 29 October 2020
Available online 3 November 2020
1385-8947/

electrodes [31–35]. Therefore, it is urgently needed to design novel kinds of mechanically durable PTCDA-based cathode materials with hierarchical conductive architectures for simultaneously enhancing the ionic/electronic transport properties and improving the reaction kinetics in SIBs.

Different from synthetic architectures, the delicate multi-scale microchannels in natural materials, such as shell [36], bone [37,38], and wood [39,40], have been demonstrated to efficiently transport water as well as the dissolved ions during the metabolism process. As illustrated in Fig. 1a, the efficient storage and transport of ions and water in wood can be ascribed to the ultra-strong capillarity within its hierarchical microchannels. This provides endless inspiration in developing electrode materials with bio-inspired hierarchical porous structures, which could significantly accelerate the mass/ion transport while retain good mechanical strength and flexibility [41,42]. Therefore, we have developed a novel organic cathode material consisting of PTCDA/nitrogen-doped carbon/carbon nanotubes (PTCDA/NC/CNT) via electrospinning and heat treatment (Fig. 1b), which well mimics the hierarchical microchannels of natural wood to achieve excellent mechanical properties. Consequently, the flexible PTCDA/NC/CNT composite nanofiber membrane possesses three-dimensional (3D) interconnected conductive frameworks, which provide rapid electron transfer pathways and maintain the structural stability during long-time electrochemical cycles. Additionally, the strong capillarity of the hierarchical micro/nanotunnels inside each porous nanofiber can largely facilitate Na^+ transport according to the equation $h = 2\gamma\cos\alpha/(\rho g R\sin\theta)$as shown in Fig. 1c, thus leading to shortened Na^+ diffusion distance and efficient utilization of PTCDA. As a result, the PTCDA/NC/CNT cathode exhibits a relatively high specific capacity of 135.6 mA h g^{-1} at a current density of 50 mA g^{-1}, a superior rate capability of 74 mA h g^{-1} at an ultra-high current density of 5000 mA g^{-1}, a super-long cycle life with very stable reversible capacity of 99 mA h g^{-1} after 500 cycles at 1000 mA g^{-1} and good mechanical flexibility of 99.1% elongation at break after 100 bending cycles. Furthermore, an all-organic rechargeable sodium-ion full battery has been constructed using the robust PTCDA/NC/CNT cathode and conjugated sodium carboxylate/carbon nanotubes (Na_4-PTC/CNT) anode, which delivers an excellent rate capability of 36 mA h g^{-1} at an ultra-high current density of 2000 mA g^{-1} and a remarkably high specific energy density of 85 W h kg^{-1} at the power density of 665 W kg^{-1}. Therefore, this bio-inspired design may pave a new way to develop high-performance organic cathodes with significantly improved mechanical properties, rapid reaction kinetics and excellent electrochemical performances for SIB applications.

2. Experimental section

2.1. Materials

3,4,9,10-perylenetetracarboxylic dianhydride (denoted as PTCDA-pre) was obtained from TCI, Tokyo Chemical Industry Co., Ltd, Tokyo,

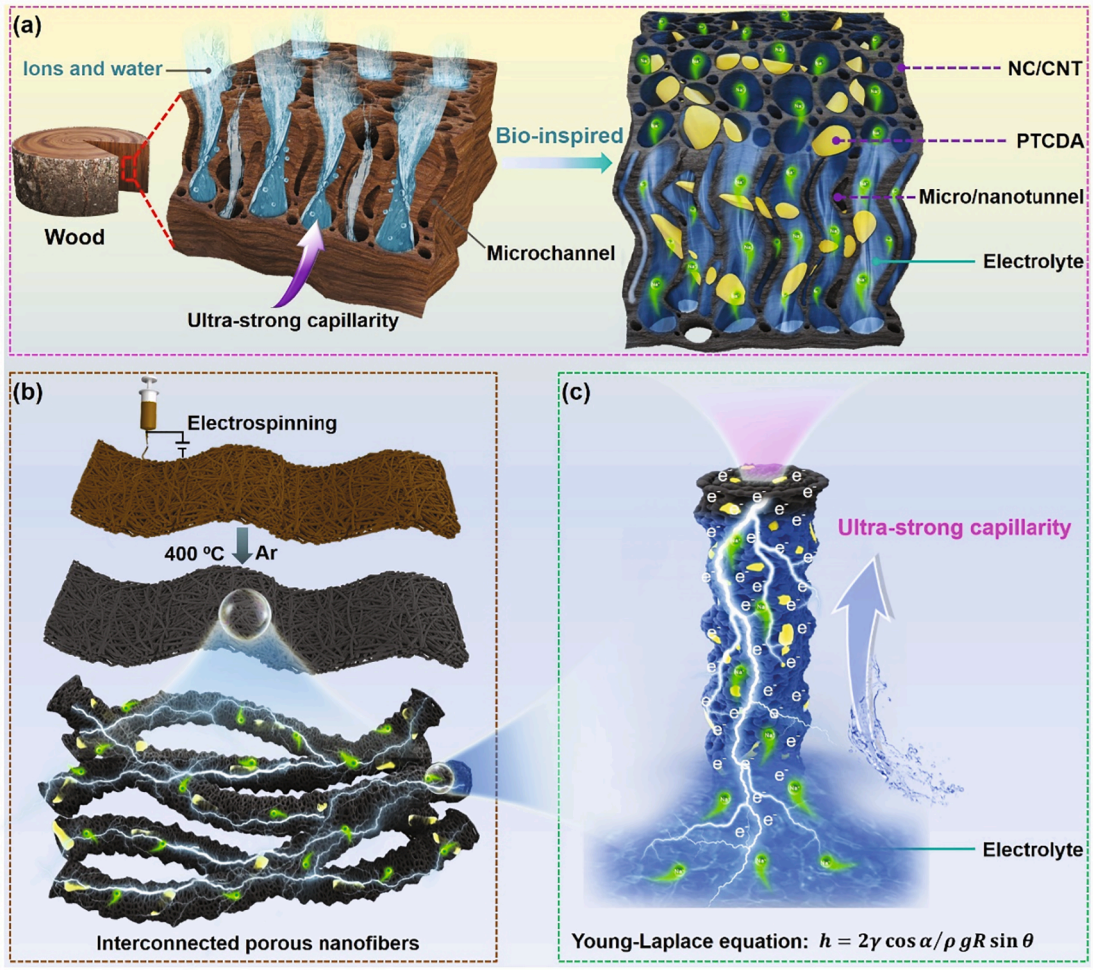

Fig. 1. (a) Schematic illustration showing the design concept of the PTCDA/NC/CNT electrode inspired by the ultra-strong capillarity of wood's hierarchical microchannels. (b) The preparation procedure of the PTCDA/NC/CNT electrode. (c) Schematic illustration of the ultra-fast Na^+ transport in a single porous PTCDA/NC/CNT nanofiber because of the ultra-strong capillary phenomenon.

Japan. Polyacrylonitrile (PAN, M_w = 86000), polymethyl methacrylate (PMMA, M_w = 350000), sodium hydroxide (NaOH) and *N,N*-dimethylformamide (DMF, 99.9%) were purchased from Sigma Aldrich. Carbon nanotubes (CNT, 10–20 nm in diameter and 10–30 μm in length) were supplied by Chengdu Institute of Organic Chemistry, Chinese Academy of Sciences, China. The elastomer prepolymer of polydimethylsiloxane (PDMS, Sylgard 184) was purchased from Dow Corning. Deionized (DI) water was used throughout all experiments. All of the reagents were analytical grade and used without further purification.

2.2. Fabrication of PTCDA/NC/CNT, PTCDA/NC, NC/CNT and PTCDA/NC/CNT-powder materials

CNT was first surface-modified by a mixture of H_2SO_4/HNO_3 (3/1, v/v). Then, 0.6 g of CNT was dispersed in 30.0 g of DMF by sonication in a 40 kHz ultrasonic bath for 10 h. Afterwards, 1.25 g of PTCDA-pre, 1.2 g of PMMA and 0.25 g of PAN were added into the above 10.0 g CNT dispersion solution under Ar atmosphere and magnetically stirred for 10 h at room temperature to obtain PTCDA-pre/PAN/PMMA/CNT dispersion solution, which was electrospun into nanofiber membrane by applying an electrical potential of 15 kV. The as-obtained nanofiber membrane was dried at 80 °C in a vacuum oven for 10 h, and followed by heat-treated at 400 °C under Ar for another 2 h for carbonization to obtain the PTCDA/NC/CNT nanofiber membrane. The exact loading amount of PTCDA in the PTCDA/NC/CNT composite was fixed at 60% based on the thermogravimetric analysis. For comparison, the composite membranes of PTCDA/NC (without CNT) and NC/CNT (without PTCDA) were also prepared via the same operation processes, respectively. The as-obtained PTCDA-pre/PAN/PMMA/CNT dispersion solution was casted on a plate glass and dried at 80 °C in a vacuum oven for 10 h, which was then heat-treated at 400 °C under Ar for another 2 h to obtain the carbonized PTCDA/NC/CNT-powder.

2.3. Fabrication of the Na_4-PTC/CNT anode

Conjugated sodium carboxylate was synthesized through a one-pot hydrolysis/sodiation reaction of PTCDA-pre to yield the corresponding tetra-sodium salt. Briefly, 3.92 g of PTCDA was poured in 200 mL of DI water. Firstly, 2.4 g of NaOH was dissolved in 50 mL of DI water, and then it was added dropwise into the above PTCDA suspension within 2 h. After stirring at room-temperature for 24 h, the red suspension turns into deep orange. The orange powder was obtained by centrifuged, washed with deionized water and acetone, and dried under vacuum at 60 °C for 10 h. To fabricate Na_4-PTC/CNT membrane, 16 mg of modified CNT and 24 mg of Na_4-PTC powder were dispersed in 20 mL of deionized water by sonication in a 40 kHz ultrasonic bath for 2 h. Then, 20 mL of the above uniform dispersion solution was vacuum-filtrated through a polyester filter membrane with an average pore diameter of 2.5 μm to generate a filter cake, which was dried at 60 °C in a vacuum oven for 10 h to obtain the Na_4-PTC/CNT composite membrane. As a result, the mass loading of the active Na_4-PTC was set as 60%. Then, this Na_4-PTC/CNT membrane was stored in an argon-filled glove box to avoid water adsorption. The sodiation was carried out by discharging the Na_4-PTC/CNT electrode to a full capacity (0.1 V *vs.* Na^+/Na) in a half-cell configuration. Then, the sodiated Na_4-PTC/CNT membrane was recycled and directly used as the anode to assemble the full battery inside an argon-filled glove box.

2.4. Characterizations

Morphologies of the PTCDA-pre/NC/CNT and PTCDA/NC/CNT membranes were observed using field-emission scanning electron microscope (FESEM, HitachiS-8010, Japan) and transmission electron microscope (TEM, Talos F200S, Thermo Fisher, USA). Chemical structures and compositions of the samples were characterized by Fourier transform infrared (FTIR, NicoletIn10MX/Nicolet6700, Thermo Fisher, USA), X-ray photoelectron spectroscopy (XPS, ESCALAB 250Xi, Thermo Fisher, USA), and ^{13}C nuclear magnetic resonance (^{13}C NMR, Bruker-Avance 400, Switzerland). The crystalline structures of the samples were detected by using powder X-ray diffraction (XRD, Bruker D8 Advance, Germany). Meanwhile, the constituent was characterized by thermogravimetric analyzer (TGA, NETZSCH TG 209 F1 Libra®, Germany) with a temperature ramp of 10 °C min^{-1} under N_2 atmosphere. The Raman spectrum of carbonaceous NC/CNT membrane has been tested by a Renishaw inVia with a laser wavelength of 532 nm. Mechanical property of the PTCDA/NC/CNT membrane was measured by a universal testing machine (SANS, Shenzhen, China) at a tensile speed of 5 mm min^{-1}. Nanoparticle size and Zeta potential analyzer (Litersizer500, Anton Paar, Austria) were used to measure the surface charge of PTCDA/NC/CNT nanofibers at various electrolyte concentrations. Electrical conductivity of the PTCDA/NC/CNT membrane was measured by a four-point probe resistivity measurement system (RST-8 model, Guangzhou four-point probe technology Co., LTD, China). Contact angles of the samples toward electrolyte were measured using a contact angle goniometer (OCA40Micro, DataPhysics Instruments GmbH, Germany) equipped with a high-speed CCD camera via the sessile and pendant drop method. The Brunauer-Emmett-Teller (BET) surface area of the samples were determined by an ASAP 2020 analyzer based on the nitrogen adsorption-desorption isotherm, while the pore width distribution was calculated based on density functional theory (DFT) model. To evaluate the nanofluidic behavior of the PTCDA/NC/CNT, NC/CNT and PTCDA/NC, a self-made testing device was fabricated consisting of a glass substrate with polydimethylsiloxane (PDMS). Typically, the PTCDA/NC/CNT membrane was glued to a glass substrate with PDMS. Then, two stainless steel strips were attached on the two ends of the device to maintain good contact. Then, the ionic conductivity was measured based on electrochemical impedance spectroscopy after soaking electrolytes of various concentrations for 12 h.

2.5. Electrochemical tests

The PTCDA/NC/CNT and Na_4-PTC/CNT membranes were cut into round slices with a diameter of 12 mm and 14 mm, respectively, and directly used as electrodes without using binder or additives to assemble CR2032 coin-type batteries. For SIBs, a metallic sodium foil was used as the counter electrode, 1 M $NaClO_4$ in EC:DMC (1:1, v/v) with 5.0% FEC as the electrolyte, and a glass fiber (Whatman) as the separator. All of the batteries were assembled in an argon-filled glove box with moisture and oxygen content below 0.1 ppm. The flexible full battery was assembled using the sodiated Na_4-PTC/CNT as anode and the PTCDA/NC/CNT nanofiber membrane as cathode. Herein, PDMS elastomer was used as the sealing agent, which was a mass ratio of 10:1, and then heat-treated at 130 °C for 30 min in a convection oven. The galvanostatic discharge/charge experiments and cyclic voltammetry (CV) tests were conducted on a battery-testing system (Land CT-2001A, Wuhan, China) and an Arbin Instruments testing system (Arbin-SCTS, USA), respectively. Electrochemical impedance spectroscopy (EIS, 0.01 Hz–100 kHz, 5 mV) measurement was performed on an electrochemical workstation (CHI 760D, China). Galvanostatic intermittent titration technique (GITT, Land CT-2001A) was applied to detect Na^+ diffusion coefficient for PTCDA/NC/CNT electrodes in SIBs. The assembled SIBs were firstly discharged and charged for ten cycles at a constant current density of 50 mA g^{-1} before GITT measurement to eliminate the influence from the formation of SEI films. Then, the battery was tested at a low current density of 10 mA g^{-1} for an intermittent time of 0.25 h followed by an open-circuit stand for 0.5 h to allow the cell potentials to relax to its steady-state value (E_s). This procedure was repeated for the full voltage operation window. In addition, all of the batteries were held at open circuits at room temperature for 12 h before electrochemical tests. The specific capacities were calculated based on the weight of active materials. The energy density of a full battery was calculated according to the

following Eq. (1):

$$E = Q \times U \quad (1)$$

where E is the energy density (W h kg^{-1}), Q is the discharge specific capacity (A h kg^{-1}), U is the corresponding average operational voltage.

3. Results and discussion

To construct the bio-inspired hierarchical micro/nanotunnels with interconnected conductive frameworks, the composite solution consisting of PTCDA-pre, PMMA and PAN as the spinning precursor and template, and CNT as the conductive agent was electrospun to prepare the PTCDA-pre/PAN/PMMA/CNT nanofiber membrane. Then, PTCDA-pre/PAN/PMMA/CNT was converted into PTCDA/NC/CNT after heat treatment at 400 °C. As analyzed by the thermogravimetric analysis (Fig. S1a), the PTCDA-pre and CNT maintain stable at 400 °C while PAN and PMMA decompose to different degrees. The exact loading amount of PTCDA in the PTCDA/NC/CNT composite is calculated to be 60% based on the different weight losses of PAN, PMMA and PTCDA-pre/PAN/PMMA/CNT after heat-treated at 400 °C. ^{13}C nuclear magnetic resonance (Fig. S1b) and FTIR spectra (Fig. S1c) further indicate that the functional groups in PTCDA-pre are well retained after treated at 400 °C. Moreover, typical diffraction peaks at 2θ = 9.5°, 12.4°, 24.5° and 27.5° can be observed in the XRD patterns of PTCDA-pre, PTCDA and PTCDA/NC/CNT composite (Fig. S1d), revealing the good structural stability of PTCDA. In order to evaluate the defective degree of the carbonaceous NC/CNT membrane, Raman spectrum of NC/CNT was obtained in Fig. S2. The Raman spectrum of NC/CNT shows both D (1343 cm^{-1}), G (1580 cm^{-1}) and 2D (2685 cm^{-1}) bands. The I_D/I_G value of NC/CNT is 1.16, indicating a low degree of defect in NC/CNT. Additionally, the presence of the 2D band in NC/CNT further indicates a certain amount of sp^2-hybridized carbon in NC/CNT membrane, which can be attributed to the introduction of CNT. Therefore, benefitting from the good dispersion of CNT, the PTCDA/NC/CNT composite nanofiber membrane still exhibits a high electrical conductivity despite the low carbonization temperature at 400 ℃, which is also consistent with the in-plane conductivity in Fig. 2g.

Morphologies of PTCDA-pre/PAN/PMMA/CNT, NC/CNT and PTCDA/NC/CNT nanofiber membranes were detected by SEM. As shown in Fig. S3a, the PTCDA-pre/PAN/PMMA/CNT nanofiber membrane forms a crosslinked network structure with uniform nanofibers. Besides, PTCDA-pre particles and CNT are evenly embedded in the PTCDA-pre/PAN/PMMA/CNT composite nanofibers (Fig. S3b). After heat treatment of PTCDA-pre/PAN/PMMA/CNT and PAN/PMMA/CNT

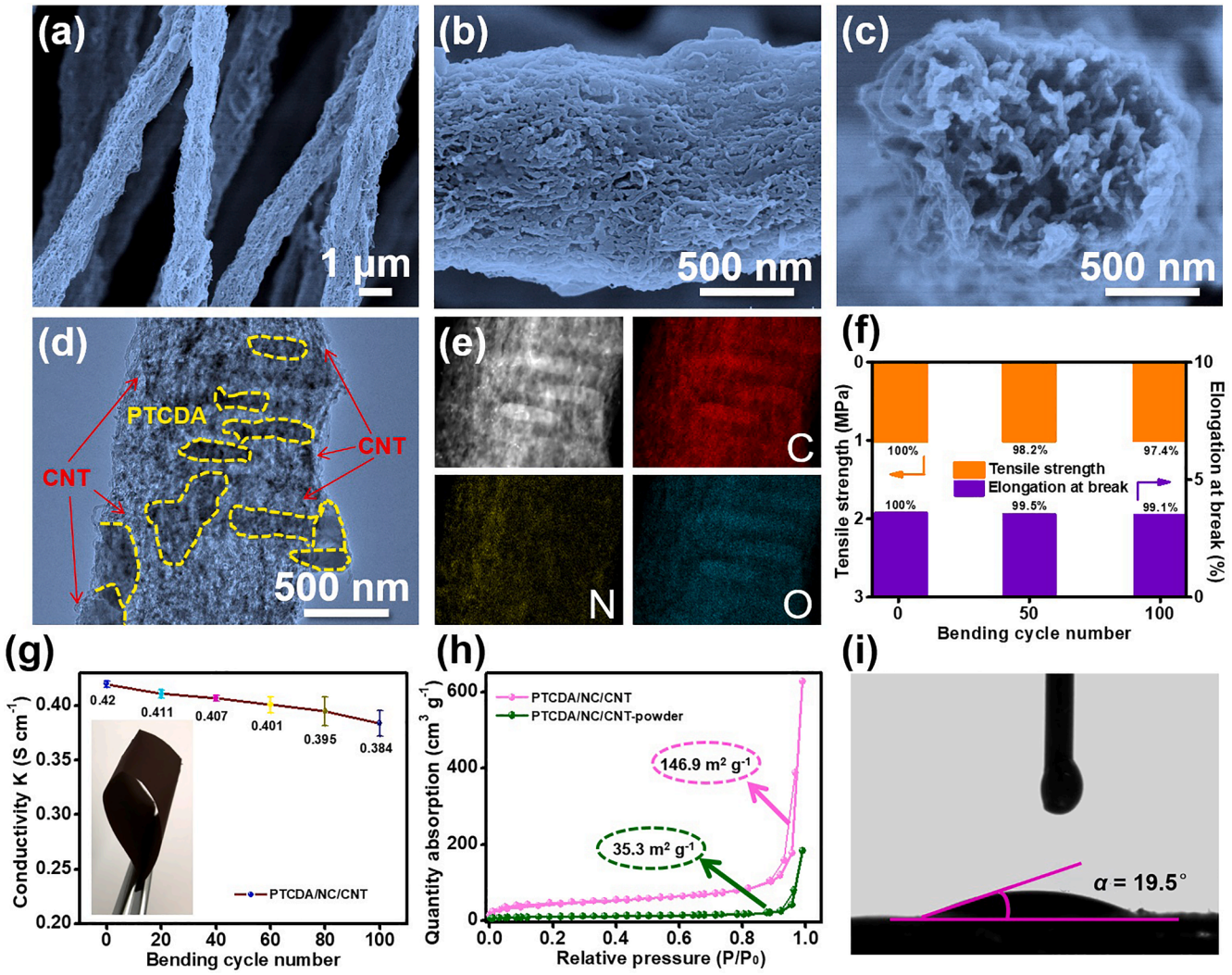

Fig. 2. Characterizations of the PTCDA/NC/CNT nanofiber membrane: (a–c) SEM, (d) TEM, and (e) the corresponding elemental mapping images. (f) Mechanical properties and (g) electrical conductivity after different bending cycles. The inset in (g) shows the flexibility of the nanofiber membrane. (h) N_2 adsorption-desorption isotherms of PTCDA/NC/CNT nanofiber membrane and PTCDA/NC/CNT-powder. (i) The contact angle of electrolyte on the surface of PTCDA/NC/CNT nanofiber membrane.

at 400 °C, the PTCDA/NC/CNT composite nanofibers with numerous hierarchical micro/nanotunnels still pile up a 3D interconnected network structure (Fig. 2a-2c). Similarly, the NC/CNT nanofibers without PTCDA particles also maintain porous structure (Fig. S3c). TEM images (Fig. 2d and S3d) further demonstrate that PTCDA particles are uniformly embedded within the porous PTCDA/NC/CNT nanofibers while deep intertwining can be observed between NC/CNT and PTCDA to form numerous interconnected micro/nanotunnels inside each nanofiber. Moreover, C, N and O elements are uniformly distributed in a single nanofiber (Fig. 2e), indicating the good combination of PTCDA, CNT and NC. As a result, the PTCDA/NC/CNT nanofiber membrane exhibits excellent mechanical flexibility with 99.1% elongation at break and good shape retention even after 100 bending cycles (Fig. 2f and S4a; Table S1), as well as a high in-plane conductivity of 0.384 S cm^{-1} after 100 bending cycles (Fig. 2g), indicating its great potential in serving as a flexible cathode without binders and conductive additives. Meanwhile, the PTCDA/NC/CNT nanofiber membrane exhibits much higher specific surface area (146.9 m^2 g^{-1}) and narrower pore size distribution compared to PTCDA/NC/CNT-powder obtained by the traditional coating method (Fig. 2h and S4b). Benefitting from numerous micro/nanotunnels inside each nanofiber, the capillarity of electrolyte in a single PTCDA/NC/CNT nanofiber can be analyzed by the following Young-Laplace Eq. (2) [43].

$$\rho g h \times sin\theta = \frac{2\gamma cos\alpha}{R} \tag{2}$$

where ρ, g and h represent the density of electrolyte, the gravitational acceleration and the increased height of electrolyte level in PTCDA/NC/CNT driven by the capillary force, respectively. γ is the surface tension of electrolyte. α is the contact angle of PTCDA/NC/CNT surface to electrolyte. R is the inner radius of the micro/nanotunnels in PTCDA/NC/CNT nanofibers. In our experiment, the γ value of sodium ion electrolyte is 18.7 × 10^{-3} N m^{-1} based on the contact angle analysis using the pendant drop method. The α value is experimentally measured to be 19.5° (Fig. 2i), ρ is ~1.294 × 10^3 kg m^{-3}, g is 9.8 m s^{-2}, R is measured to be ~850 × 10^{-9} m by SEM (Fig. 2c), and θ is between 0 and 90°. Thus, the value of h can be calculated as following:

$$h = 3.26/sin\theta \tag{3}$$

The minimum value of h can reach 3.26 m based on Eq. (3), which is much higher than the actual length of PTCDA/NC/CNT nanofibers. This result theoretically demonstrates that the PTCDA/NC/CNT nanofibers possess ultra-strong capillarity to enhance the ability of absorbing and storing the electrolyte, thereby greatly improving the transport of Na^+ inside PTCDA/NC/CNT during the electrochemical cycles as illustrated in Fig. 1c.

Based on the above mentioned advantages, the as-designed PTCDA/NC/CNT cathode is highly expected with superior electrochemical performances. Fig. 3a shows the typical CV curves between 1.5 and 3.5 V (*vs* Na/Na^+) at a scan rate of 0.1 mV s^{-1}. The CV curves show a pair of reduction peaks at 2.14 V and 2.06 V with two shoulders around 2.27 V and 1.98 V, and a pair of oxidation peaks at 2.59 V and 2.63 V with two shoulders around 2.11 V and 2.46 V. The highly overlapped CV curves reveal an excellent reversible stability during the electrochemical reactions. The voltage profiles also demonstrate two serial discharge voltage plateaus at 2.14 V and 2.06 V as well as two charge voltage plateaus at 2.59 V and 2.63 V (Fig. 3b), which are quite consistent with the CV results. This should be ascribed to the formation of the radical anion ($PTCDA^-$) and radical dianion ($PTCDA^{2-}$) during the redox processes as shown in Fig. 3c, corresponding to the sequential one-electron reduction processes or two-electron reduction processes of PTCDA with Na^+ as previously reported [26,30,44,45]. Meanwhile, the PTCDA/NC/CNT cathode also delivers an outstanding discharge capacity of 135.6 mA h g^{-1} at 50 mA g^{-1}, indicating its great potential as an advanced cathode in SIBs. For comparison, the CV and galvanostatic discharge/charge curves of NC/CNT cathode are displayed in Fig. S5. Obviously, no redox peak appears in NC/CNT electrode and the capacity of NC/CNT can be almost neglected, which well demonstrates that the NC/CNT composite only acts as a stable and conductive skeleton.

In order to understand the storage mechanism of the PTCDA/NC/

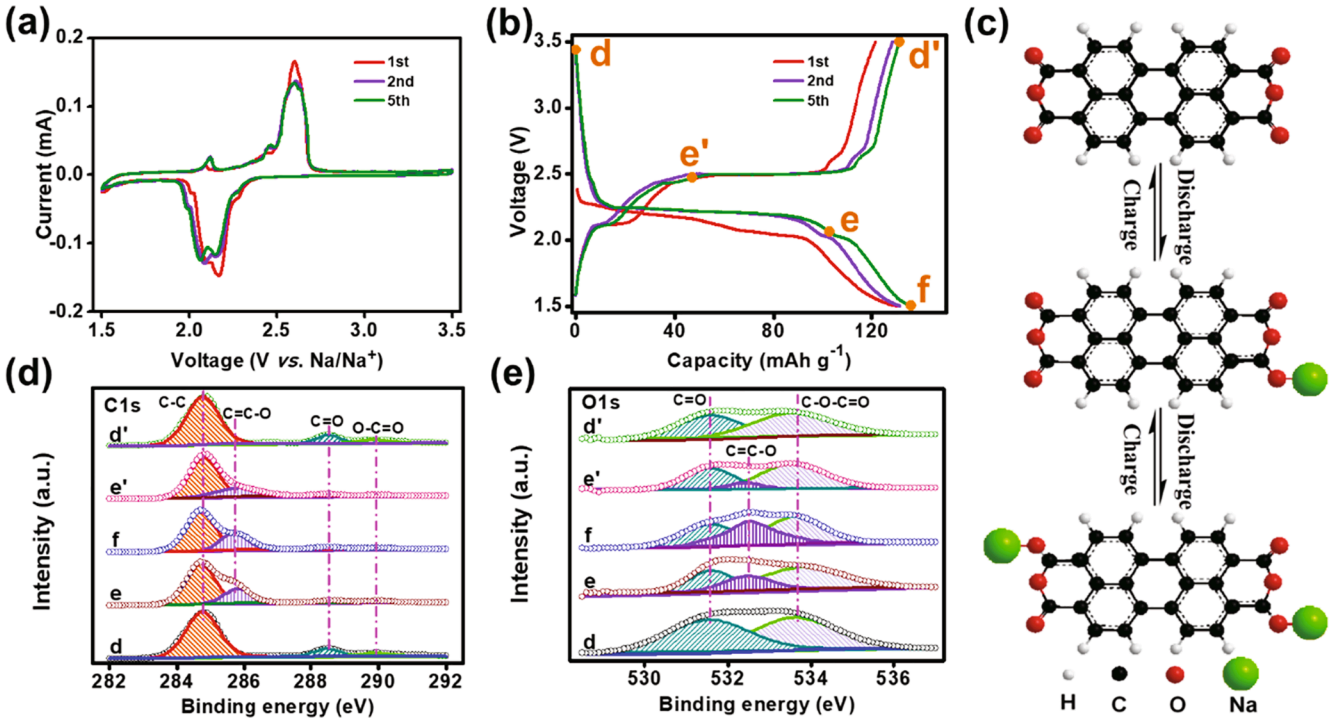

Fig. 3. Electrochemical analysis of PTCDA/NC/CNT cathode in SIBs: (a) CV at a scan rate of 0.1 mV s^{-1} and (b) galvanostatic discharge/charge curves at a current density of 50 mA g^{-1}. The inset points in (b): different discharge/charge states. (c) The most possible redox mechanisms of PTCDA in SIBs. (d, e) *Ex-situ* XPS spectra corresponding to the inset points in Fig. 3b, respectively.

CNT cathode with Na^+ in SIBs, *ex-situ* XPS measurement was conducted corresponding to different discharge/charge positions (Fig. 3b). As shown in Fig. 3d, the relative intensities of C═O (288.5 eV) and O–C═O (290.0 eV) peaks gradually decrease from point *d* to *f* and a new peak related to C═C–O–Na (285.6 eV) appears in the C 1s spectrum. Conversely, the relative intensities of C═O and O–C═O peaks increase gradually and the peak assigned to C═C–O–Na disappears when the electrode is fully charged from point *f* to *d*′. Additionally, the peak corresponding to the carbonyl group (C═O) becomes broad and weak at the discharged state (point *f*) and a new peak arises at 532.5 eV in the O 1s spectrum during the discharge process (Fig. 3e), indicating the formation of a new bond (C═C–O–Na) between the carbonyl groups (C═O) and sodium ions [26,31]. After recharged back to 3.5 V (point *d*′), the C═C–O–Na peak disappears accompanied by the intensity increase of C═O (531.6 eV) and C–O–C═O (533.5 eV) peaks to the original states, revealing the reversible transformation between C–C═O and C═C–O–Na bonds during the discharge/charge processes (Fig. S6). This result is coincident with the reported theoretical mechanism of carbonyl groups storing Na^+ [26,30,31,45].

Additionally, a broad peak around 1631 cm^{-1} appears after fully discharging (point *f*) and then disappears when recharging (point *d*′) in the *ex-situ* FTIR spectra (Fig. 4a), further indicating the reversible redox reactions of PTCDA with Na^+ [26,31]. Besides, the *ex-situ* XRD was also conducted to elucidate the structural evolution of PTCDA with Na^+ insertion/extraction during the discharge/charge processes (Fig. S7). It can be seen that all of the peaks at $2\theta = 12.4°$ (021), 24.8° (042) and 27.6° (102) shift to lower angles and the peak at $2\theta = 9.2°$ (011) nearly disappears after sodiation (point *f*), while all peaks return to the original positions after fully charging. This suggests a reversible change of molecular structure between PTCDA and Na^+ during the sodiation/desodiation processes. Moreover, the *ex-situ* SEM and TEM images also indicate that the PTCDA/NC/CNT cathode maintains the original morphology with interconnected micro/nanotunnel structures (Fig. 4b and c). Abundant C, N, O and Na elements can be observed obviously on the PTCDA/NC/CNT cathode after 500 cycles (Fig. 4d), further confirming the good structural stability and efficient utilization of PTCDA in

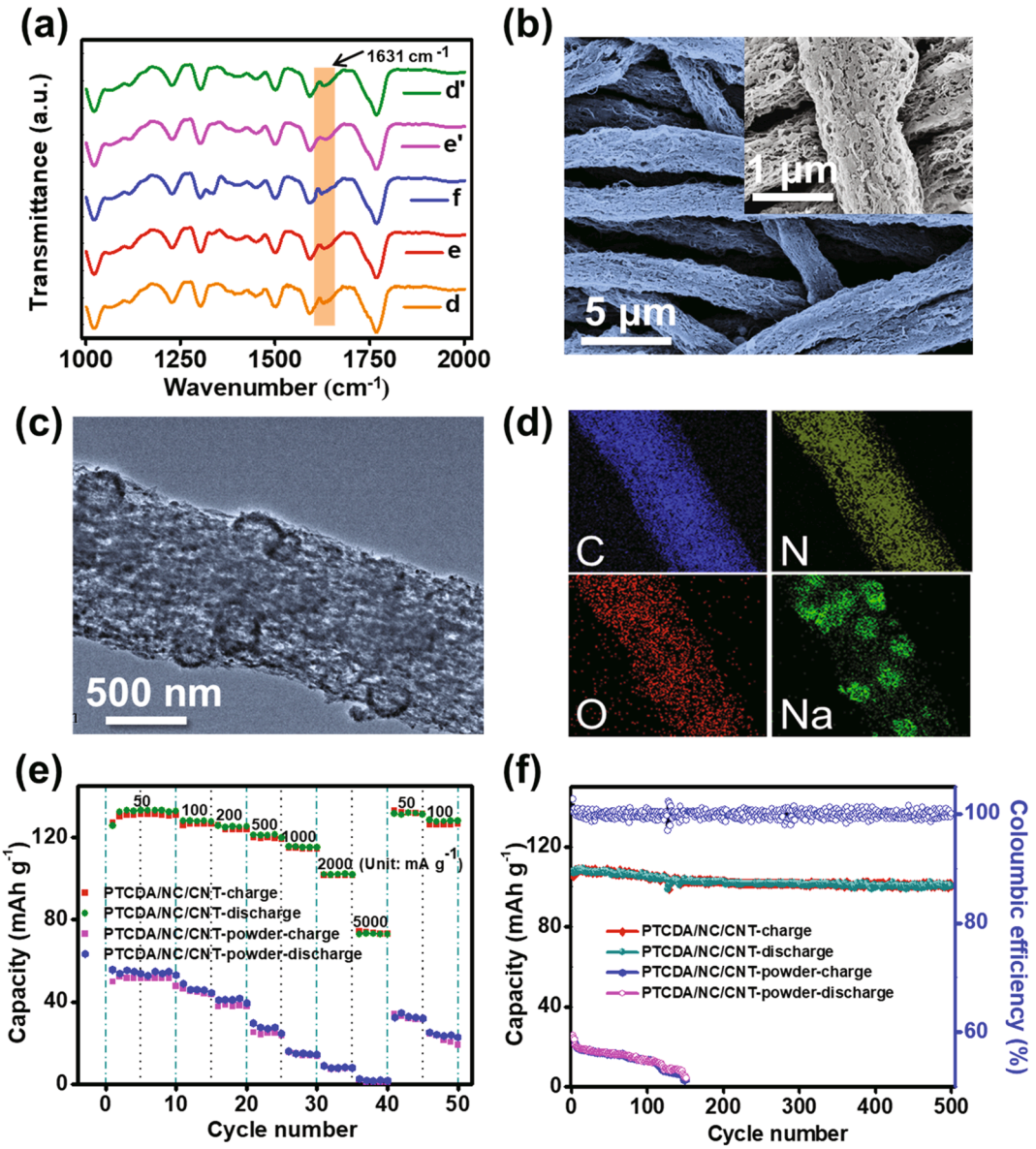

Fig. 4. (a) *Ex-situ* FTIR spectra corresponding to the inset points in Fig. 3b. (b) *Ex-situ* SEM, (c) TEM images, and (d) the corresponding EDS mappings of carbon, nitrogen, oxygen and sodium of the PTCDA/NC/CNT cathode after 500 cycles in SIBs. (e) Rate performance and (f) cycling stability of different electrodes at a current density of 1000 mA g^{-1}, respectively.

SIBs. As a result, the PTCDA/NC/CNT cathode delivers an excellent rate performance with an ultrahigh reversible capacity of 74 mA h g^{-1} at a high current density of 5000 mA g^{-1} (Fig. 4e), which is much higher than that of the PTCDA/NC/CNT-powder and PTCDA/NC electrodes (Fig. S8). Besides, the capacity could recover its initial value easily even after cycling at high current density over 5000 mA g^{-1} (Fig. 4e), indicating good stability of the PTCDA/NC/CNT cathode during fast discharge/charge processes. Meanwhile, the PTCDA/NC/CNT cathode exhibits an ultra-stable reversible capacity of 99 mA h g^{-1} with an average Coulombic efficiency approaching 100% after 500 cycles at 1000 mA g^{-1} (Fig. 4f). In sharp contrast, the capacity and rate performance of PTCDA/NC/CNT-powder and PTCDA/NC electrodes decay distinctly under all current densities because of the agglomeration of PTCDA/NC/CNT-powder (Fig. S9a–c) and the low conductivity of PTCDA/NC nanofiber membrane (Fig. S9d–f and Table S2). In addition, the assembled sodium-ion half cell based on PTCDA/NC/CNT cathode exhibits much higher specific capacity and rate capability than those of most previously reported sodium-ion half cells incorporating other PTCDA-based cathodes (Table S3). The excellent electrochemical performances of the PTCDA/NC/CNT cathode should be ascribed to the interconnected conductive frameworks and ultra-strong capillarity contributed by numerous micro/nanotunnels inside each nanofiber, which provide rapid migration paths for electrons and short diffusion distance of Na^+, and thus render the efficient utilization and structural stability of PTCDA during the electrochemical reactions.

The Na^+ storage mechanism and reaction kinetics are further investigated by CV at different scan rates to verify the advantages of the PTCDA/NC/CNT cathode in SIBs. As shown in Fig. 5a, the CV curves exhibit typical redox peaks and maintain similar shapes with the increase of scan rate, indicating little polarization and excellent electrochemical reaction kinetics of the electrode during the successive discharge/charge processes. Moreover, all of the CV curves feature symmetric redox peaks from 0.1 to 0.5 mV s^{-1} and both of the anodic and cathodic peak currents (i_p) are proportional to the square root of the scan rate ($v^{0.5}$) as shown in Fig. S10. Then, a high diffusion coefficient of Na^+ (8.15×10^{-13} cm^2 s^{-1}) is calculated according to the Randles-Sevcik equation (see the calculation details in Supporting Information), further confirming the rapid Na^+ transport property. Besides, to distinguish the Na^+ storage mechanism of diffusion-controlled (intercalated) or capacitive process, a typical analysis of the CV curves at various scan rates was conducted based on the following equation [46,47]:

$$i = av^b \tag{4}$$

where the current i as a function of potential obeys a power law relationship with the scan rate (v). a and b are the adjustable parameters.

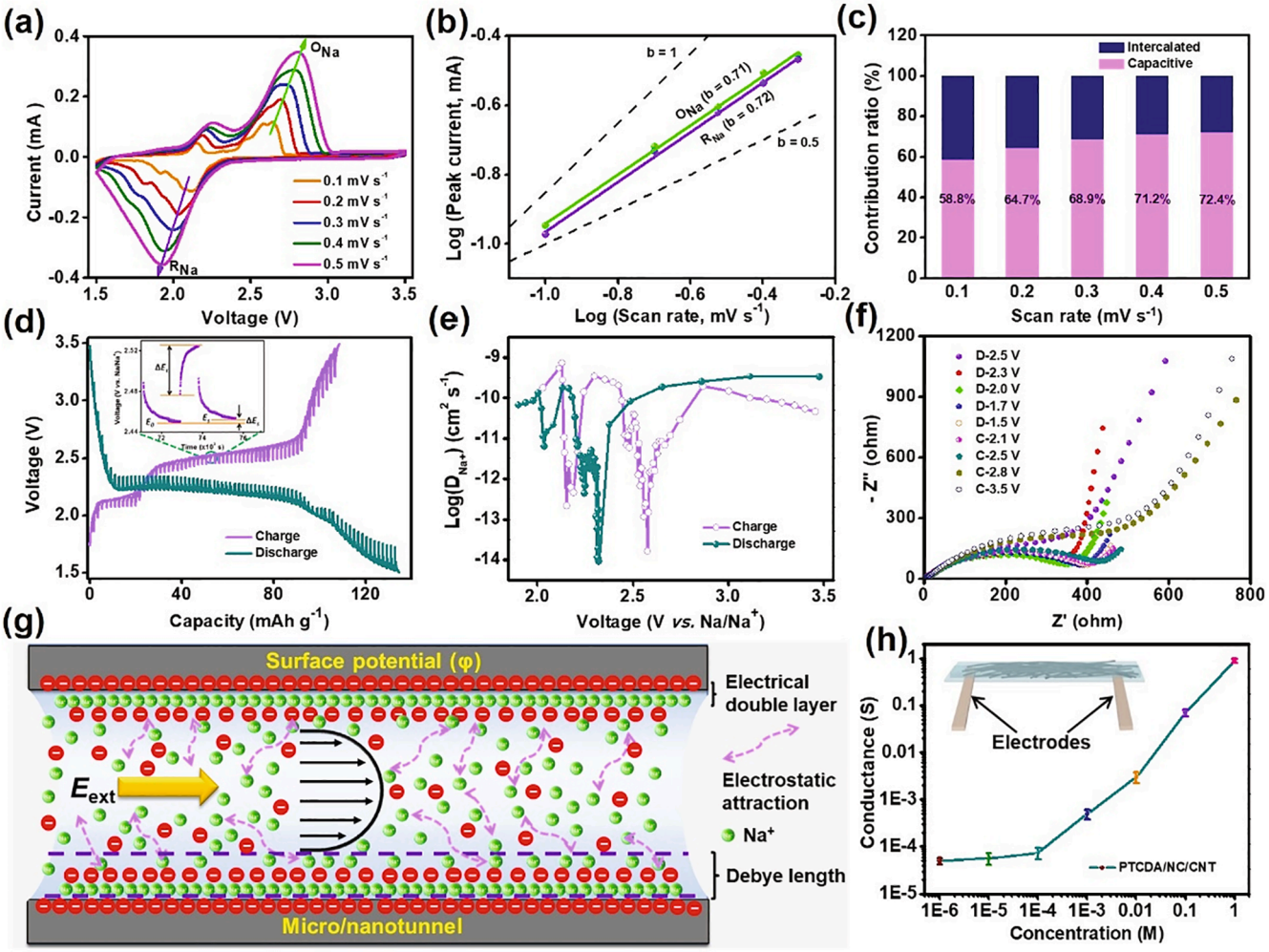

Fig. 5. Electrochemical mechanism analysis of PTCDA/NC/CNT cathode in SIBs: (a) CV curves, (b) *b*-values analysis, (c) normalized contribution ratios at different scan rates, and (d) GITT curves. Inset of (d): voltage profiles for a single step of GITT at ~2.48 V during charging. (e) Na^+ diffusion coefficients (D_{GITT}) calculated from GITT. (f) Nyquist plots at different discharge/charge states. (g) Schematic illustration of the ion transport behavior in a negatively charged micro/nanochannel. $\boldsymbol{E}_{ext}$ denotes the external electric field. (h) Ionic conductivity as a function of electrolyte concentration. The inset in (h) illustrates the ionic conductivity measurement.

The value of b can be determined from the slope of the plots of log (i) versus log (v), as described in the following equation:

$$\log(i) = b \times \log(v) + \log(a) \quad (5)$$

The b value of 1 indicates a capacitive process, while b value of 0.5 represents a diffusion-controlled process. According to the linear relationship between log (i) versus log (v) plots, b values of the cathodic peak (R_{Na}) and anodic peak (O_{Na}) are calculated as 0.72 and 0.71, respectively (Fig. 5b). This implies that the PTCDA/NC/CNT cathode includes both diffusion-controlled (intercalated) process and capacitive contribution. In further, the qualitative analysis was performed to determinate the contribution ratios between the two mechanisms for PTCDA/NC/CNT cathode at different scan rates based on the following equations:

$$i(\mathrm{V}) = k_1\nu + k_2\nu^{\frac{1}{2}} \quad (6)$$

$$i(\mathrm{V})/\nu^{\frac{1}{2}} = k_1\nu^{\frac{1}{2}} + k_2 \quad (7)$$

where $k_1\nu$ and $k_2\nu^{\frac{1}{2}}$represent the surface capacitive effects and diffusion-controlled process, respectively. The parameters of k_1 and k_2 are determined from the linear relationship of $i(\mathrm{V})/\nu^{\frac{1}{2}}$ and $\nu^{\frac{1}{2}}$ based on Eq. (7). The detailed results for this calculation are shown in Fig. S11a and S11b, while a typical capacitive contribution area (shadowed) is observed for the CV curve of the PTCDA/NC/CNT cathode at 0.3 mV s^{-1} in Fig. S11c. The ratios of capacitive contribution and diffusion-controlled process at various scan rates are summarized in Fig. 5c. The histogram shows that the capacitive contribution increases with the increase of scan rate, which should be responsible for the excellent rate performance of PTCDA/NC/CNT-based SIBs.

Galvanostatic intermittent titration technique (GITT) measurement was carried out to estimate the diffusion coefficients of Na^+ (D_{GITT}) in the PTCDA/NC/CNT cathode for SIBs (Fig. 5d). The evolution of the quasi-equilibrium potential *vs.* × (stoichiometry of Na^+) in PTCDA is obtained from the GITT results as shown in Fig. S12a, while the corresponding differential factors (dE/dx) are shown in Fig. S12b. The voltage varies a little in the plateau stage and the dE/dx values are approximate to zero, which is consistent with the theoretical analysis [48]. Since the electrochemical diffusion process of Na^+ follows the Fick's second law [48,49], the D_{GITT} values are obtained within the range from 10^{-14} to 10^{-9} cm^2 S^{-1} (Fig. 5e) based on the GITT analysis results (see the calculation details in Supporting Information). Electrochemical impedance spectroscopy (EIS) is another efficient method to measure the chemical diffusion coefficient. Performed under the open circuit at different discharge/charge states, all of the Nyquist plots of the PTCDA/NC/CNT cathode exhibit relatively similar shape with a semicircle in the high-frequency region and a sloping line in the low-frequency region (Fig. 5f), demonstrating that the electrochemical behavior is controlled by both charge transfer and ion diffusion processes. According to the model proposed by Ho et al. [50,51], the diffusion coefficients of Na^+ (D_{EIS}) for the PTCDA/NC/CNT cathode can be calculated based on the EIS results (with the calculation details shown in Supporting Information). As exhibited in Fig. S13b, the D_{EIS} values are in the range from 10^{-14} to 10^{-9} cm^2 S^{-1}, which are consistent with the results obtained by GITT and CV analyses. In order to further explain the high diffusion coefficients of Na^+, Na^+ transport behavior in the nanofibrous micro/nanotunnels has been further analyzed theoretically. Encouragingly, the surface of the bio-inspired hierarchical micro/nanotunnels is proved to be negatively charged by the zeta potential of PTCDA/NC/CNT nanofiber dispersion (Fig. S14). According to the theoretical model of ion transport in a negatively charged micro/nanotunnel as shown in Fig. 5g (with the theoretical analysis details in Supporting Information), Na^+ transport can be accelerated in the negatively charged environment driven by the external electric field (E_{ext}), thereby achieving the high sodium ionic conductance under various electrolyte concentrations. Consequently, PTCDA/NC/CNT nanofiber membrane achieves higher sodium ionic conductance than that of PTCDA/NC nanofiber membrane (Fig. 5h and S15). These results fully demonstrate that the PTCDA/NC/CNT cathode possesses a superior rate performance and ultra-long cyclic stability in SIBs attributed to the rapid ionic/electronic transport, high diffusion coefficients of Na^+ and ultrafast reaction kinetics benefiting from the interconnected conductive frameworks and ultra-strong capillarity of the negatively charged hierarchical micro/nanotunnels.

In order to explore the practical application of the PTCDA/NC/CNT cathode in green and sustainable rechargeable SIBs, a metallic sodium-free full organic battery was assembled (Fig. 6a), using the PTCDA/NC/CNT cathode coupled with an anode of flexible conjugated sodium carboxylate/carbon nanotubes (Na_4-PTC/CNT) composite (see the preparation details in experimental section). As shown in Fig. S16, CNT tangle and interweave with Na_4-PTC sheets, constructing interconnected and long-range conducting networks for the as-prepared Na_4-PTC/CNT composite anode with an overall thickness around 70 μm. The Na_4-PTC/CNT composite anode exhibits good mechanical flexibility with a high discharge capacity of 125.5 mA h g^{-1}, excellent rate performance and good cycle stability in SIBs (Fig. S16b and S18). Besides, low charge-transfer impedance and high diffusion coefficients of Na^+ have been achieved for the assembled SIBs with Na_4-PTC/CNT electrodes (Fig. S19). The full organic battery of PTCDA/NC/CNT//Na_4-PTC/CNT with an optimized weight ratio of 1:1.2 between the cathode and anode materials was tested from 0.8 V to 3.0 V. As shown in Fig. 6b, the CV curves show an anodic peak at 1.75 V with a shoulder around 1.49 V, and a cathodic peak at 1.52 V with a shoulder around 1.21 V, respectively. Meanwhile, the full battery exhibits an obvious voltage plateau with a high initial discharge capacity of 134.5 mA h g^{-1} at the current density of 10 mA g^{-1} (Fig. 6c) and excellent rate performance of 36 mA h g^{-1} at a high current density of 2000 mA g^{-1} (Fig. 6d and S20). The high specific capacity and excellent rate performance can be attributed to the low polarization and ultrafast Na^+ transport between the electrode and electrolyte, which are also confirmed by the low charge-transfer impedance and small Warburg coefficient of the full battery (Fig. 6e and f). In particular, the full battery displays an ultra-stable cycling performance with a high Coulombic efficiency of 99% and a capacity of 64 mA h g^{-1} after 200 cycles at 200 mA g^{-1}, which could turn on a light emitting diode (LED) (Fig. 6g). Notably, the as-prepared all-organic sodium-ion battery exhibits much higher energy density and power density than those of most previously reported sodium-ion full battery devices (Fig. 6h) [52–54], indicating great potential of PTCDA/NC/CNT as a high-performance cathode material for the next-generation green and sustainable rechargeable SIBs.

4. Conclusions

In summary, we have innovatively designed and constructed a flexible PTCDA/NC/CNT cathode with interconnected conductive frameworks and negatively charged hierarchical micro/nanotunnels inspired by the unique hierarchical microchannels of natural wood for superior stable all-organic rechargeable sodium-ion battery applications. The as-prepared PTCDA/NC/CNT cathode exhibits excellent mechanical stability and high in-plane conductivity. Meanwhile, this biomimetic structure can enhance the diffusion kinetics of Na^+, shorten the diffusion distance of Na^+ and improve the electrode conductivity, thus inducing the resultant SIBs with high reversible capacity, superior rate performance and excellent cycling stability. Besides, the assembled all-organic rechargeable sodium-ion battery with robust PTCDA/NC/CNT cathode and Na_4-PTC/CNT anode delivers a high specific energy density of 85 W h kg^{-1} at the power density of 665 W kg^{-1}, which is much superior over those of most previous sodium-ion full batteries. Therefore, we believe this unparalleled structural design inspired by nature will provide a new strategy to develop green and sustainable organic electrodes for robust and ultrafast energy-storage devices.

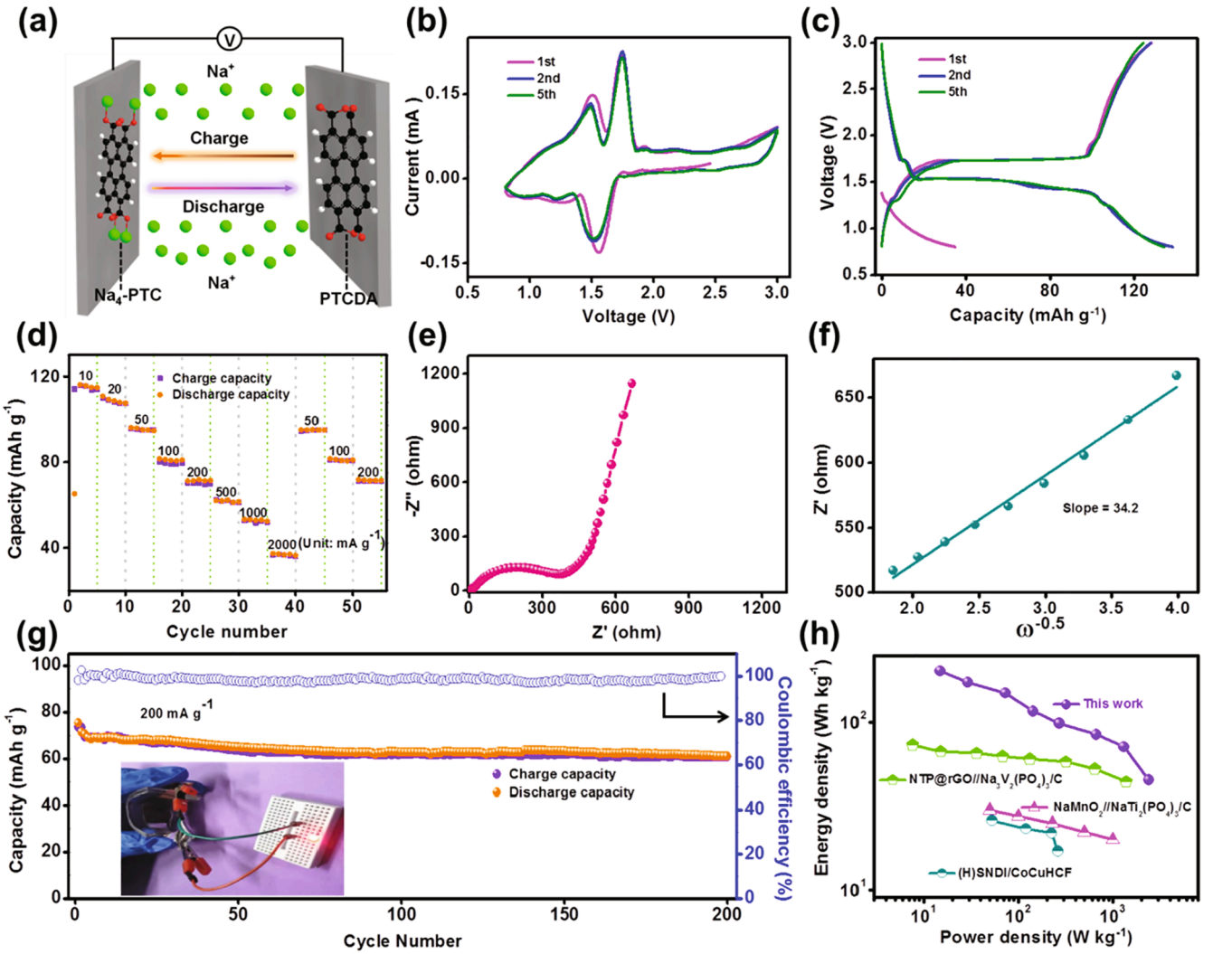

Fig. 6. Electrochemical performances of the flexible all-organic sodium-ion battery: (a) Schematic architecture, (b) CV curves at a scan rate of 0.1 mV s^{-1}, (c) galvanostatic discharge/charge curves at a current density of 10 mA g^{-1}, (d) rate performance, (e) Nyquist plot, (f) linear relationship between Z′ versus $\omega^{-0.5}$ and (g) cycling performance. (h) Ragone plots of this work compared to other previously reported sodium-ion full batteries.

Declaration of Competing Interest

The authors declare that they have no known competing financial interests or personal relationships that could have appeared to influence the work reported in this paper.

Acknowledgements

The authors are grateful for the financial support from the Natural Science Foundation of Shanghai (18ZR1401600), "Chenguang Program" supported by Shanghai Education Development Foundation and Shanghai Municipal Education Commission (16CG39), Shanghai Scientific and Technological Innovation Project (18JC1410600), and Fundamental Research Funds for the Central Universities and Graduate Student Innovation Fund of Donghua University (CUSF-DH-D-2019006).

Appendix A. Supplementary data

Supplementary data to this article can be found online at https://doi.org/10.1016/j.cej.2020.127597.

References

[1] Y. Yan, S. Xia, H. Sun, Y. Pang, J. Yang, S. Zheng, A promising 3D crystalline red P/reduced graphene oxide aerogel architecture anode for sodium-ion batteries, Chem. Eng. J 393 (2020), 124788.
[2] H. Lim, H. Kim, S.O. Kim, W. Choi, Self-assembled N-doped MoS_2/carbon spheres by naturally occurring acid-catalyzed reaction for improved sodium-ion batteries, Chem. Eng. J 387 (2020), 124144.
[3] Y. Jiang, Z.Z. Yang, W.H. Li, L.C. Zeng, F.S. Pan, M. Wang, X. Wei, G.T. Hu, L. Gu, Y. Yu, Nanoconfined carbon-coated $Na_3V_2(PO_4)_3$ particles in mesoporous carbon enabling ultralong cycle life for sodium-ion batteries, Adv. Energy Mater. 5 (2015) 1402104.
[4] S. Chen, F. Wu, L. Shen, Y. Huang, S.K. Sinha, V. Srot, P.A. van Aken, J. Maier, Y. Yu, Cross-linking hollow carbon sheet encapsulated CuP 2 nanocomposites for high energy density sodium-ion batteries, ACS Nano 12 (7) (2018) 7018–7027.
[5] J. Sun, H.-W. Lee, M. Pasta, H. Yuan, G. Zheng, Y. Sun, Y. Li, Y.i. Cui, A phosphorene–graphene hybrid material as a high-capacity anode for sodium-ion batteries, Nat. Nanotechnol. 10 (11) (2015) 980–985.
[6] Z. Liu, L.H. Zhang, L.Z. Sheng, Q.H. Zhou, T. Wei, J. Feng, Z.J. Fan, Edge-nitrogen-rich carbon dots pillared graphene blocks with ultrahigh volumetric/gravimetric capacities and ultralong life for sodium-ion storage, Adv. Energy Mater. 8 (2018) 1802042.
[7] Y. Fang, X.-Y. Yu, X.W. Lou, Nanostructured electrode materials for advanced sodium-ion batteries, Matter 1 (1) (2019) 90–114.
[8] S. Yang, Y. Cheng, X. Xiao, H. Pang, Development and application of carbon fiber in batteries, Chem. Eng. J 384 (2020), 123294.
[9] S. Chen, C. Wu, L. Shen, C. Zhu, Y. Huang, K. Xi, J. Maier, Y. Yu, Challenges and perspectives for NASICON-type electrode materials for advanced sodium-ion batteries, Adv. Mater. 29 (2017) 1700431.

[10] G.L. Xu, R. Amine, A. Abouimrane, H.Y. Che, M. Dahbi, Z.F. Ma, I. Saadoune, J. Alami, W.L. Mattis, F. Pan, Z.H. Chen, K. Amine, Challenges in developing electrodes, electrolytes, and diagnostics tools to understand and advance sodium-ion batteries, Adv. Energy Mater. 8 (2018) 1702403.

[11] J.-Y. Hwang, S.-T. Myung, Y.-K. Sun, Sodium-ion batteries: present and future, Chem. Soc. Rev. 46 (12) (2017) 3529–3614.

[12] L. Li, Y. Zheng, S.L. Zhang, J.P. Yang, Z.P. Shao, Z.P. Guo, Recent progress on sodium ion batteries: potential high-performance anodes, Energy Environ. Sci. 11 (2018) 2310–2340.

[13] H. Wang, T. Yao, C. Li, L. Meng, Y. Cheng, Constructing three-dimensional ordered porous MoS_2/C hierarchies for excellent high-rate long-life pseudocapacitive sodium storage, Chem. Eng. J. 397 (2020), 125385.

[14] H. Huang, R. Xu, Y. Feng, S. Zeng, Y. Jiang, H. Wang, W. Luo, Y. Yu, Sodium/potassium-ion batteries: boosting the rate capability and cycle life by combining morphology, defect and structure engineering, Adv. Mater. 32 (2020) 1904320.

[15] Y. Subramanian, W. Oh, W. Choi, H. Lee, M. Jeong, R. Thangavel, W.S. Yoon, Optimizing high voltage $Na_3V_2(PO_4)_2F_3$ cathode for achieving high rate sodium-ion batteries with long cycle life, Chem. Eng. J 403 (2021), 126291.

[16] Y. Liang, Z. Tao, J. Chen, Organic electrode materials for rechargeable lithium batteries, Adv. Energy Mater. 2 (7) (2012) 742–769.

[17] T.B. Schon, B.T. McAllister, P.-F. Li, D.S. Seferos, The rise of organic electrode materials for energy storage, Chem. Soc. Rev. 45 (22) (2016) 6345–6404.

[18] J.S. Park, S. Yang, Y.C. Kang, Prussian blue analogue nanocubes with hollow interior and porous walls encapsulated within reduced graphene oxide nanosheets and their sodium-ion storage performances, Chem. Eng. J 393 (2020), 124606.

[19] Q. Liu, Z. Hu, M. Chen, C. Zou, H. Jin, S. Wang, S.L. Chou, Y. Liu, S.X. Dou, The cathode choice for commercialization of sodium-ion batteries: layered transition metal oxides versus prussian blue analogs, Adv. Funct. Mater. 30 (2020) 1909530.

[20] T. Ma, Q. Zhao, J. Wang, Z. Pan, J. Chen, A sulfur heterocyclic quinone cathode and a multifunctional binder for a high-performance rechargeable lithium-ion battery, Angew. Chem. Int. Ed. 55 (22) (2016) 6428–6432.

[21] M. Wu, Y. Cui, A. Bhargav, Y. Losovyj, A. Siegel, M. Agarwal, Y. Ma, Y. Fu, Organotrisulfide: a high capacity cathode material for rechargeable lithium batteries, Angew. Chem. Int. Ed. 55 (2016) 10027–10031.

[22] Q. Zhao, Y. Lu, J. Chen, Advanced organic electrode materials for rechargeable sodium-ion batteries, Adv. Energy Mater. 7 (2017) 1601792.

[23] J. Zhang, K. Zhang, J.H. Yang, G.H. Lee, J. Shin, V.H. Lau, Y.M. Kang, Bifunctional conducting polymer coated CoP core-shell nanowires on carbon paper as a free-standing anode for sodium ion batteries, Adv. Energy Mater. 8 (2018) 1800283.

[24] S. Wu, W. Wang, M. Li, L. Cao, F. Lyu, M. Yang, Z. Wang, Y. Shi, B. Nan, S. Yu, Z. Sun, Y. Liu, Z. Lu, Highly durable organic electrode for sodium-ion batteries via a stabilized a-C radical intermediate, Nat. Commun. 7 (2016) 13318.

[25] S. Bahceci, B. Esat, A polyacetylene derivative with pendant TEMPO group as cathode material for rechargeable batteries, J. Power Sour. 242 (2013) 33–40.

[26] G.Y. Zhou, Y.E. Miao, Z.X. Wei, L.L. Mo, F.L. Lai, Y. Wu, J.M. Ma, T.X. Liu, Bioinspired micro/nanofluidic ion transport channels for organic cathodes in high-rate and ultrastable lithium/sodium-ion batteries, Adv. Funct. Mater. 28 (2018) 1804629.

[27] Y. Wang, Y.u. Ding, L. Pan, Y.e. Shi, Z. Yue, Y.i. Shi, G. Yu, Understanding the size-dependent sodium storage properties of Na 2 C 6 O 6 -based organic electrodes for sodium-ion batteries, Nano Lett. 16 (5) (2016) 3329–3334.

[28] Y. Zhang, Y. An, S. Dong, J. Jiang, H. Dou, X. Zhang, Enhanced cycle performance of polyimide cathode using a quasi-solid-state electrolyte, J. Phys. Chem. C 122 (39) (2018) 22294–22300.

[29] S. Gu, S. Wu, L. Cao, M. Li, N. Qin, J. Zhu, Z. Wang, Y. Li, Z. Li, J. Chen, Z. Lu, Tunable redox chemistry and stability of radical intermediates in 2D covalent organic frameworks for high performance sodium ion batteries, J. Am. Chem. Soc. 141 (24) (2019) 9623–9628.

[30] L. Cui, L. Zhou, K. Zhang, F. Xiong, S. Tan, M. Li, Q. An, Y.M. Kang, L. Mai, Salt-controlled dissolution in pigment cathode for high-capacity and long-life magnesium organic batteries, Nano Energy 65 (2019), 103902.

[31] W. Luo, M. Allen, V. Raju, X. Ji, An organic pigment as a high-performance cathode for sodium-ion batteries, Adv. Energy Mater. 4 (2014) 1400554.

[32] H.-G. Wang, S. Yuan, Z. Si, X.-b. Zhang, Multi-ring aromatic carbonyl compounds enabling high capacity and stable performance of sodium-organic batteries, Energy Environ. Sci. 8 (11) (2015) 3160–3165.

[33] H. Banda, D. Damien, K. Nagarajan, M. Hariharan, M.M. Shaijumon, A polyimide based all-organic sodium ion battery, J. Mater. Chem. A 3 (19) (2015) 10453–10458.

[34] W. Deng, Y. Shen, J. Qian, Y. Cao, H. Yang, A perylene diimide crystal with high capacity and stable cyclability for na-ion batteries, ACS Appl. Mater. Interfaces 7 (38) (2015) 21095–21099.

[35] T.B. Schon, A.J. Tilley, E.L. Kynaston, D.S. Seferos, Three-dimensional arylene diimide frameworks for highly stable lithium ion batteries, ACS Appl. Mater. Interfaces 9 (18) (2017) 15631–15637.

[36] U.G.K. Wegst, H. Bai, E. Saiz, A.P. Tomsia, R.O. Ritchie, Bioinspired structural materials, Nat. Mater. 14 (1) (2015) 23–36.

[37] H.D. Espinosa, J.E. Rim, F. Barthelat, M.J. Buehler, Merger of structure and material in nacre and bone – perspectives on de novo biomimetic materials, Prog. Mater. Sci. 54 (8) (2009) 1059–1100.

[38] S. Weiner, W. Traub, H.D. Wagner, Lamellar bone: structure-function relations, J. Struct. Biol. 126 (1999) 241–255.

[39] M. Zhu, J. Song, T. Li, A. Gong, Y. Wang, J. Dai, Y. Yao, W. Luo, D. Henderson, L. Hu, Highly anisotropic, highly transparent wood composites, Adv. Mater. 28 (26) (2016) 5181–5187.

[40] F. Shen, W. Luo, J.Q. Dai, Y.G. Yao, M.W. Zhu, E. Hitz, Y.F. Tang, Y.F. Chen, V. L. Sprenkle, X.L. Li, L.B. Hu, Ultra-thick, low-tortuosity, and mesoporous wood carbon anode for high-performance sodium-ion batteries, Adv. Energy Mater. 6 (2016) 1600377.

[41] J. Peng, Q. Cheng, High-performance nanocomposites inspired by nature, Adv. Mater. 29 (2017) 1702959.

[42] L. Min, H. Pan, S. Chen, C. Wang, N.ü. Wang, J. Zhang, Y. Cao, X. Chen, X.u. Hou, Recent progress in bio-inspired electrospun materials, Compos. Commun. 11 (2019) 12–20.

[43] Y.S. Joung, C.R. Buie, Aerosol generation by raindrop impact on soil, Nat. Commun. 6 (2015) 6083.

[44] M. Tang, S.L. Zhu, Z.T. Liu, C. Jiang, Y.C. Wu, H.Y. Li, B. Wang, E.J. Wang, J. Ma, C.L. Wang, Tailoring p-conjugated systems: from p-p stacking to high-rate-performance organic cathodes, Chem 4 (2018) 1–15.

[45] H. Wang, P. Hu, J. Yang, G. Gong, L. Guo, X. Chen, Renewable-Juglone-based high-performance sodium-ion batteries, Adv. Mater. 27 (14) (2015) 2348–2354.

[46] K. Ma, H. Jiang, Y.J. Hu, C.Z. Li, 2D nanospace confined synthesis of pseudocapacitance-dominated MoS_2-in-Ti_3C_2 superstructure for ultrafast and stable Li/Na-ion batteries, Adv. Funct. Mater. 28 (2018) 1804306.

[47] Y. Yao, M. Chen, R. Xu, S. Zeng, H. Yang, S. Ye, F. Liu, X. Wu, Y. Yu, CNT interwoven nitrogen and oxygen dual-doped porous carbon nanosheets as free-standing electrodes for high-performance Na-Se and K-Se flexible batteries, Adv. Mater. 30 (2018) 1805234.

[48] K. Tang, X. Yu, J. Sun, H. Li, X. Huang, Kinetic analysis on $LiFePO_4$ thin films by CV, GITT, and EIS, Electrochim. Acta 56 (13) (2011) 4869–4875.

[49] Y.Y. Wang, B.H. Hou, J.Z. Guo, Q.L. Ning, W.L. Pang, J.W. Wang, C.L. Lü, X.L. Wu, An ultralong lifespan and low-temperature workable sodium-ion full battery for stationary energy storage, Adv. Energy Mater. 8 (2018) 1703252.

[50] C. Ho, I.D. Raistrick, R.A. Huggins, Application of A-C techniques to the study of lithium diffusion in tungsten trioxide thin films, J. Electrochem. Soc. 127 (2) (1980) 343–350.

[51] S. Yang, X. Wang, X. Yang, Y. Bai, Z. Liu, H. Shu, Q. Wei, Determination of the chemical diffusion coefficient of lithium ions in spherical $Li[Ni_{0.5}Mn_{0.3}Co_{0.2}]O_2$, Electrochim. Acta 66 (2012) 88–93.

[52] Y. Fang, L. Xiao, J. Qian, Y. Cao, X. Ai, Y. Huang, H. Yang, 3D Graphene decorated $NaTi_2(PO_4)_3$ microspheres as a superior high-rate and ultracycle-stable anode material for sodium ion batteries, Adv. Energy Mater. 6 (2016) 1502197.

[53] Z. Hou, X. Li, J. Liang, Y. Zhu, Y. Qian, An aqueous rechargeable sodium ion battery based on a NaMnO 2 –NaTi 2 (PO 4) 3 hybrid system for stationary energy storage, J. Mater. Chem. A 3 (4) (2015) 1400–1404.

[54] D.J. Kim, Y.H. Jung, K.K. Bharathi, S.H. Je, D.K. Kim, A. Coskun, J.W. Choi, An aqueous sodium ion hybrid battery incorporating an organic compound and a Prussian blue derivative, Adv. Energy Mater. 4 (2014) 1400133.